## PAPER

Check for updates

# Fast assembly of 'clickable nanogels' for drug delivery†

Pasquale Mastella, ID *[ab] Aldo Moscardini,[a] Andrea Guerrini[a] and Stefano Luin ID [ac]

Poly(α-glutamic acid) (PGA)-based nanogels (NGs) have garnered significant attention due to their biocompatibility, biodegradability, and potential to be functionalized. Recent advances in click chemistry, particularly strain-promoted azide−alkyne cycloaddition (SPAAC), enable the formation of nanogels under mild, metal-free conditions, preserving biocompatibility and avoiding contamination. In this work, we developed and optimized a protocol based on SPAAC click chemistry for the production of PGA-based NGs; moreover, we investigated their physicochemical properties, stability, and potential for drug delivery by encapsulating doxorubicin (Dox) as a model drug. The produced NGs showed high stability under various storage conditions, especially when containing the drug. We observed sustained drug release in various buffers or media, retention of drug functionality in cell cultures, and its transfer to cell nuclei with a delay of few hours with respect to the free drug. This click-chemistry-based method for NG production can be easily applied to produce different nanostructures, and the original or modified nanogels could serve as carriers not only for hydrophilic drugs, but also for proteins or other biomolecules in a variety of biomedical applications.

Nanogels (NGs) are an emerging class of nanostructured materials with exceptional versatility, finding applications in drug delivery, diagnostics, and regenerative medicine.[1–3] These hydrophilic nanoparticles are formed by a three-dimensional, highly crosslinked polymer network with a high capacity to hold water, enabling the efficient encapsulation and controlled release of bioactive molecules. Their properties such as size, charge, porosity, softness, amphiphilic character, and degradability can be adjusted to address a wide range of biological applications by varying their chemical composition, *e.g.* the used polymers and cross-linking agents. Crosslinking in NGs can be achieved through various mechanisms, including physical interactions[4] or covalent bonds (*e.g.*, disulfide bridges, Schiff base linkages, or click chemistry reactions).[5,6] Physically crosslinked nanogels rely on reversible interactions such as hydrogen bonding, hydrophobic forces, or ionic interactions

(*e.g.*, polyelectrolyte complexes); these systems offer simplicity and mild processing but often suffer from limited mechanical stability, poor resistance to dilution or medium exchange, and uncontrolled drug release under physiological conditions.[4,7] Chemically crosslinked nanogels such as those obtained by radical polymerization, UV-initiated curing, or copper-catalyzed azide–alkyne cycloaddition (CuAAC) achieve higher structural integrity and tunable degradation, but usually require toxic initiators, metal catalysts, or harsh synthesis conditions that may compromise encapsulated drugs or limit biocompatibility.[8]

In any case, the structural features of NGs allow them to efficiently encapsulate hydrophilic drugs, proteins, or nucleic acids, protecting them from degradation and enhancing their stability and bioavailability.[1,7] Additionally, NGs can be engineered to exhibit stimuli-responsiveness, releasing their cargo in response to specific triggers such as pH, temperature, or biological signals;[9,10] this makes them ideal for targeted and controlled therapeutic applications. Beyond their capacity to deliver traditional pharmacological agents, nanogels have emerged as versatile platforms capable of co-delivering diagnostic compounds and, as already mentioned, genetic materials. They can encapsulate imaging agents such as fluorescent dyes or MRI contrast agents, enabling real-time tracking of biodistribution and therapeutic efficacy.[11] Moreover, their adaptable polymeric network safeguards nucleic acids—including siRNA and mRNA—facilitating controlled release and efficient gene modulation for therapeutic interventions.[12] This multifunctionality positions nanogels as promising candidates in theranostics, integrating both diagnostic and therapeutic

*[a]NEST Laboratory, Scuola Normale Superiore, Piazza San Silvestro 12, 56127 Pisa, Italy. E-mail: pasquale.mastella@sns.it*

*[b]Fondazione Pisana per la Scienza ONLUS, Via Ferruccio Giovannini 13, San Giuliano Terme, 56017 Pisa, Italy*

*[c]NEST Laboratory, Istituto Nanoscienze-CNR, Piazza San Silvestro 12, 56127 Pisa, Italy*

† Electronic supplementary information (ESI) available: Chart S1: structure of the polymers used for synthesis. Scheme S1: reaction between DBCO and poly(α-glutamic acid). Scheme S2: SPAAC click reaction. Fig. S1: predicted ¹H-NMR spectra for PGA and *N*-acylisourea. Fig. S2: UV-Vis spectrum of PGA–Dox nanogel. Fig. S3: calibration curve for doxorubicin content inside nanogels. Fig. S4: confocal microscopy images of cells treated with NGs-D-647. Fig. S5: cytotoxicity study of the nanogels. Fig. S6: UV-Vis spectrum of PGA-647. See DOI: https://doi.org/10.1039/d5na00471c

functions within a single nanocarrier system. Among the various types of NGs, those based on poly-amino acids (PAAs) have gained particular attention due to their biocompatibility, biodegradability, and versatile functionalization. PAA-based NGs are often composed of naturally derived or synthetic amino acid polymers and can be fine-tuned to create materials that are bioactive and/or responsive to specific environmental stimuli. A standout example of this class of NGs is based on poly-L-glutamic acid (PGA), a hydrophilic and biodegradable polymer with numerous advantages in therapeutic applications. PGA exists in two forms: the synthetically synthesized poly(α-glutamic acid) and the naturally occurring poly(γ-glutamic acid), which are polymerized through an amidic bond involving the carboxyl group attached to the α carbon and the one at the end of the side chain, respectively. Poly(γ-glutamic acid) is produced through microbial fermentation by *Bacillus* species, as in natto, the most widely known form of the γ-isomer, derived from soybeans.[13] Poly(α-glutamic acid), despite having glutamic acid in the naturally occurring configuration found in proteins, is synthetically prepared *via* ring-opening polymerization (ROP) of glutamic acid *N*-carboxyanhydride; this production method ensures precise control over molecular weight and results in low polydispersity (~1.1).[14,15] While both poly(γ-glutamic acid) and poly(α-glutamic acid) share hydrophilicity and electrostatic interaction capabilities, the precise synthesis of poly(α-glutamic acid) makes it particularly suited for biomedical applications like drug delivery and theranostics, also because its more accessible free carboxyl groups allow easier attachment of drugs or imaging agents. A crucial property of PGA-based NGs is their complete biodegradability within the body.[16,17] When internalized by cells, PGA undergoes enzymatic degradation through lysosomal enzymes, such as cathepsin B, which break the polymer down into its monomeric form.[6] This enzymatic breakdown ensures that the nanogel is safely metabolized without accumulating in the body, a key advantage over other materials that may persist and pose long-term toxicity risks. This biodegradation process also allows for the controlled and gradual release of encapsulated drugs especially at accumulation sites for the NGs, potentially minimizing systemic side effects and improving therapeutic efficacy of the delivery system. A notable example of PGA application in NGs is OPAXIO, a paclitaxel formulation conjugated with PGA, which has progressed to advanced clinical trial stages for cancer treatment.[18] The combination of PGA biodegradability, its ability to encapsulate hydrophilic drugs, and its biocompatibility makes it an ideal choice for the development of targeted drug delivery systems.

In this article, we present an innovative approach to the formulation of PGA NGs using click chemistry, specifically the strain-promoted azide–alkyne cycloaddition (SPAAC) reaction.[8] This method enables the creation of highly controlled NGs under metal-free conditions, ensuring compatibility with biomedical applications. Moreover, we employ an inverse nanoprecipitation technique, avoiding the use of surfactants or additional crosslinking agents, which allows for the development of the cleanest possible formulation. By employing α-PGA as the polymeric backbone, our system efficiently encapsulates

doxorubicin, a widely used chemotherapeutic agent considered here as a model drug. We focus on studying the physicochemical properties of the nanogel itself and its interactions with cells, to explore its potential as a promising platform for targeted drug delivery applications.

## Results and discussion

### PGA precursor synthesis and characterization

To develop this system of click-derived PGA NGs, we used two poly(α-glutamic acid) polymers in their sodium salt form with similar molecular weights (approximately 30 000 kDa), one modified with azide (–N$_3$) and one with dibenzocyclooctyne (DBCO), two orthogonal reactive groups (PGA–N$_3$ and PGA–DBCO, in Chart S1a and b,† respectively). PGA functionalized with azide groups was commercially purchased, while PGA derivatized with DBCO was synthesized. For the latter, a DBCO molecule extended with an amine group –NH$_2$ (DBCO–amine, Scheme S1†) was conjugated to the unmodified PGA polymer (Chart S1,† panel c) through carbodiimide chemistry, achieving high yields (~75% when substituting 10% or 20% of the carboxyl groups on the polymer; see Scheme S1†). The preparation of PGA–DBCO polymers with either 10% or 20% DBCO functionalization relative to the monomeric units enabled evaluation of the effect of functional group density on subsequent nanogel formation. The successful functionalization of PGA polymers was confirmed through HPLC and UV-Vis spectroscopy, demonstrating high reaction efficiency and reproducibility (Fig. 1). In particular, in HPLC we used a column specific for water-soluble polymers and quantified the functionalization after purification *via* UV-Vis spectroscopy at 310 nm, where the DBCO ring absorbs (Fig. 1B). These analyses confirmed that the process was well-controlled, scalable, and reproducible, providing polymers suitable for further optimization and nanogel synthesis.

### NG synthesis and characterization

To optimize the coupling efficiency between PGA–N$_3$ and PGA–DBCO precursors, we evaluated various reaction conditions, focusing on factors such as the moiety ratio, reaction time, and different degrees of functionalization. For the crosslinking, we employed SPAAC (strain-promoted azide–alkyne cycloaddition), a conjugation method that does not require copper catalysts or additional reagents, making it a simpler and more biocompatible alternative to the common CuAAC (copper-catalyzed azide–alkyne cycloaddition). This allowed the development of NGs using water as the reaction solvent, ensuring a biocompatible and straightforward process. NGs were synthesized *via* inverse nanoprecipitation, also known as flash nanoprecipitation,[19] where an aqueous polymer solution was added to a water-miscible non-solvent, resulting in crosslinking within nanodroplets. We tested the different reaction conditions reported in Table 1 to produce NGs suitable for biological applications, ensuring that they had sizes around 100 nm (appropriate for drug delivery applications[20,21]) with a low polydispersity index (PDI) and that they were stable. DLS analyses revealed that the
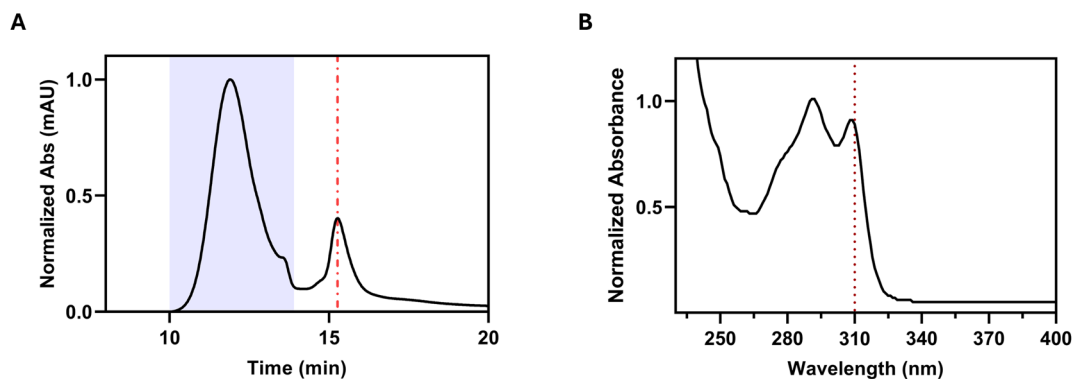
Fig. 1  (A) HPLC chromatogram illustrating the separation between the polymer conjugated with DBCO (lilac area) and the non-conjugated DBCO (red dash-dotted line). The image shows a measurement on the product of a reaction with a polymer having 10% DBCO substitution; (B) UV-Vis spectra of the PGA–DBCO conjugate exhibiting absorbance at 310 nm (red dashed line) in $H_2O$.

optimal size and PDI, along with high reproducibility and stability, were achieved with PGA–DBCO functionalized at 10% (as in PGA–$N_3$) at a 1 : 1 ratio between DBCO and $N_3$ moieties (see Table 1). In contrast, using 20% DBCO functionalization resulted in poorly stable particles at all DBCO : $N_3$ ratios, with PDI values above 0.2, indicating a less uniform size distribution and reduced reproducibility. Based on these observations, we selected the configuration labeled as entry 6 in Table 1 as the optimal formulation for subsequent experiments. This configuration with a lower degree of substitution in PGA–DBCO should also produce a more flexible polymer network and may enhance drug encapsulation and release properties.[22]

Finally, the successful chemical coupling within the NGs was confirmed through ^{1}H NMR and FT-IR spectroscopy (Fig. 2). Fig. 2A shows the ^{1}H-NMR spectra of PGA–$N_3$ and PGA–DBCO before the SPAAC reaction, together with the spectrum obtained from the PGA NGs after the reaction, all in deuterated water ($D_2O$). Many features are very similar for the three samples, but there are also some differences. The typical signals of PGA are present for all three samples: the single proton present on the methanetriyl group (α position; see also Scheme S1†) gives a signal around 4.3 ppm, the methylene group adjacent to the carboxylic group (γ position) gives a signal around 2.45 ppm and the methylene group at β-position gives a signal around 2.1 ppm, as has been observed experimentally for γ-PGA,[23,24]

and similar to the simulations reported in Fig. S1A.†[25,26] In the PGA–DBCO and NG spectra we can also identify the aromatic protons between 6.8 and 7.8 ppm typical of the DBCO group (even if not resolved), with some expected differences upon the formation of the triazole ring on that group.[27] Furthermore, in the area between 2.6 and 3.3 ppm, where PGA normally has no signals, some peaks are present in PGA–DBCO and in NGs, mostly caused by the alkyl components of the DBCO: indeed, peaks close to 2.8–2.9 and to 3.1 ppm have been reported to appear when DBCO–amine was attached by an amidic bond to a larger molecule.[28,29] In any case, we cannot rule out a contribution around 3.2 ppm from the N-acylisourea formed from the excess of EDC during the reaction for producing the PGA–DBCO (see Scheme S1†): in the predicted spectrum reported in Fig. S1B† there is a peak at this shift, and a similar peak was observed and assigned to "impurities" when EDC was used in forming amidic bonds,[24] as well as in an NMR spectrum of EDC;[30] unfortunately, it is difficult to confirm the presence of this N-acylisourea, since its ^{1}H-NMR peaks fall in regions where multiple peaks are present in the spectra reported in Fig. 2A. Only in the NG spectra, it is possible to observe a signal around 5.8 ppm, which confirms the successful coupling between the azide and the DBCO moieties.[28,29] This peak corresponds to the methylene group at the α position of the new formed triazole[31] (see Scheme S2† and the inset in Fig. 2A); in PGA–$N_3$ the

Table 1  Reaction parameters evaluated for the SPAAC coupling of PGA–$N_3$ and PGA–DBCO precursors and resulting sizes and PDIs for the NGs

| Conditions | % $N_3$/% DBCO[a] | $N_3$/DBCO molar ratio[b] | Size (nm) | PDI |
|---|---|---|---|---|
| 1 | 10/20 | 1 : 1 | 159.2 ± 1.4 | 0.123 ± 0.012 |
| 2 | 10/20 | 1 : 2 | 102.0 ± 3.2 | 0.216 ± 0.019 |
| 3 | 10/20 | 1 : 3 | NA | NA |
| 4 | 10/20 | 2 : 1 | 52.4 ± 7.0 | 0.270 ± 0.032 |
| 5 | 10/20 | 3 : 1 | NA | NA |
| 6 | 10/10 | 1 : 1 | 124.1 ± 2.0 | 0.107 ± 0.013 |
| 7 | 10/10 | 2 : 1 | 153.5 ± 1.0 | 0.700 ± 0.012 |
| 8 | 10/10 | 1 : 2 | 74.0 ± 0.6 | 0.262 ± 0.004 |

[a] Degree of functionalization of PGA polymers. [b] Molar ratio between $N_3$ (azide moieties) and DBCO (dibenzocyclooctyne moieties). In the last two columns, data are shown as averages ± SD ($n = 3$) and NA (not achieved) indicates that particle formation did not occur under the tested conditions.
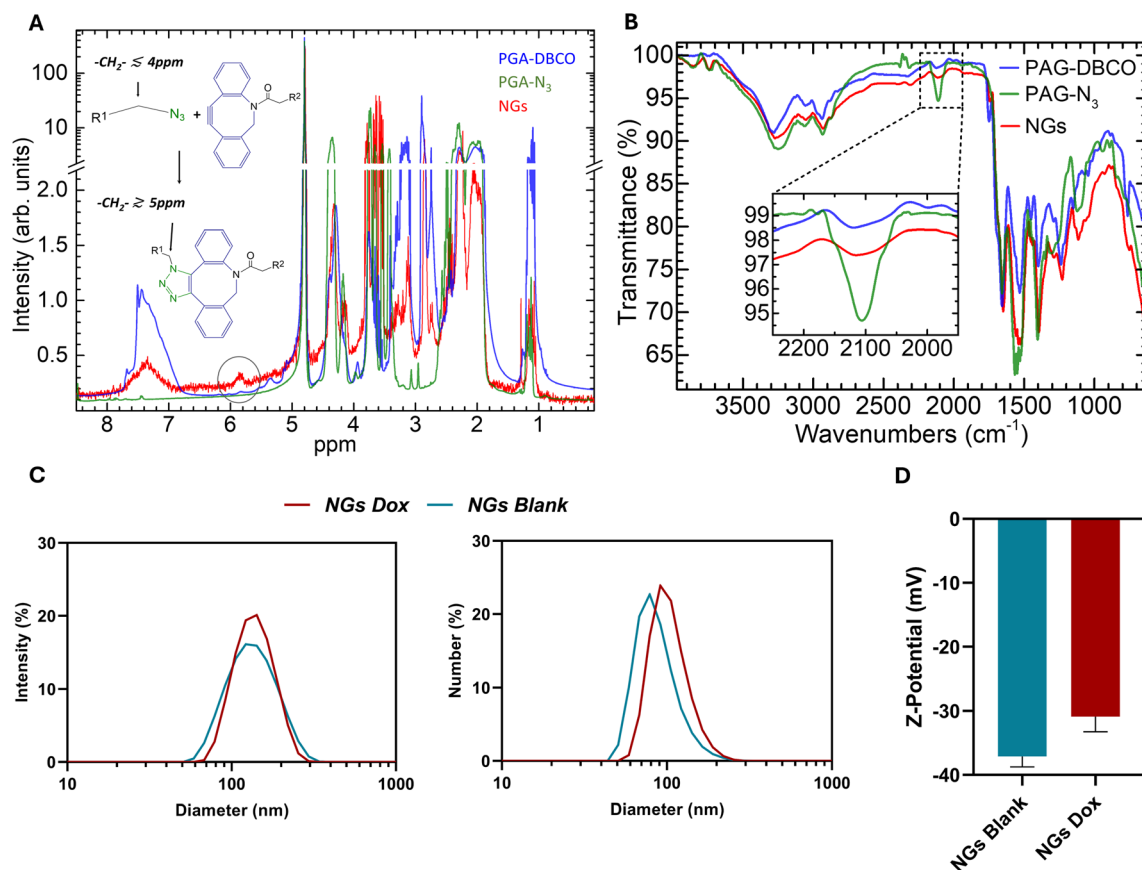
**Fig. 2** (A) $^1$H-NMR spectra (in $D_2O$) of PGA polymers before (PGA–DBCO in blue and PGA–$N_3$ in green) and after (red) SPAAC coupling and NG formation; the circle highlights the peak of the probable methylene adjacent to the triazole, as schematized in the insets. (B) FT-IR spectra showing the effect of SPAAC cross-linking in NGs (red) compared to PGA–$N_3$ (green) and PGA–DBCO (blue); the inset shows a zoomed-in view of the highlighted region, where the typical peak of –$N_3$ is present only for PGA–$N_3$. (C) Dynamic light scattering analysis comparing the particle size distributions of empty and DOX-loaded NGs weighted by intensity and by number. The distributions are averaged over three measurements for each of three different particle batches (9 measurements in total). (D) $Z$-Potential analysis of empty and Dox-loaded NGs. Data are averages ± SDs, obtained from three measurements for each of three different particle batches.

corresponding signal should be below or at about 4 ppm,[28,29] but without knowing the structure of the linker (*) in PGA–$N_3$ (Chart S1 and Scheme S2†) we cannot identify it with certainty, and it can be in the region between 3.4 and 2.9 ppm where other peaks, most probably caused by this structure, are also present in the spectra of PGA–$N_3$ and NGs.

FT-IR spectroscopy of the two starting polymers and of the resulting NGs (Fig. 2B) further confirmed crosslinking by revealing the disappearance of the characteristic azide signal at 2100 cm$^{-1}$ in the last case. The stretching mode of alkyne moieties also has a similar energy, but it cannot be IR-active because it resides in a region of DBCO with high symmetry with respect to the plane of symmetry of the C≡C bond. It is possible that some triple-bond stretching modes contribute to the weak feature around 2100 cm$^{-1}$ visible in the PGA–DBCO spectrum in Fig. 2B, and contributions from these and from unreacted azides could cause the similar structure seen in the NG IR spectrum; however the spectra are so alike (and the signal is hidden by the stronger peak in the PGA–$N_3$ one) that we cannot rule out contributions from a non-properly corrected baseline and/or from impurities. In all three samples, instead,

we can identify the typical signals of PGA: a broad signal around 3200 cm$^{-1}$ is attributable to the N–H stretching of amide and O–H stretching from carboxylic acid and residual water; the stretching of saturated C–H falls below 3000 cm$^{-1}$; the signal at 1649 cm$^{-1}$ is attributable to the stretching of C=O (in the amides) and the signals around 1540 cm$^{-1}$ are attributable to the N–H bending as well as to the stretching of C–N in the amides. We can also observe the bending of the alkyl groups around 1400 cm$^{-1}$.[23,32] The signal at 1741 cm$^{-1}$ can be attributed to the stretching of the carbonyl bond belonging to some residual protonated carboxyl groups formed under the reaction conditions used for the attachment of the DBCO molecule (at pH 6.5).[23] This explains their presence only in the PGA–DBCO and to a lesser extent in the NGs, while the PGA–$N_3$ used in the IR-absorption measurement was the powder used as supplied by the manufacturer, in sodium-salt form, and therefore the carboxyl groups are all deprotonated. Peaks eventually arising from *N*-acylisourea are difficult to recognize, because they fall in the 1520–1690 cm$^{-1}$ range, where IR lines of the amide bonds are also present.[30]

Although we cannot unequivocally confirm the presence of *N*-acylisourea in PGA–DBCO, its formation from excess EDC might influence nanogel stability. As a neutral and non-reactive by-product substituting a mostly negatively charged group ($COO^-$ at physiological pH), *N*-acylisourea might slightly alter the nanogel microenvironment, potentially attenuating repulsive electrostatic interactions amongst polymer chains and thus contributing to improved formation and stability. However, since our optimal formulation was obtained with moderate EDC excess with respect to the carboxyl groups and showed high reproducibility and stability, any such effect is likely minimal.

### Dox loading into NGs

Doxorubicin (Dox)[33] was employed as a model chemotherapeutic drug in the formulations, due to its widespread use as a standard treatment for various cancers, including breast, lung, stomach, and ovarian ones, as well as Hodgkin and non-Hodgkin lymphoma and certain types of leukemia, such as acute lymphoblastic leukemia and acute myeloid leukemia. The encapsulation of Dox occurred during the nanoprecipitation process of the clickable polymers in the organic solvent, which led to the formation of nanodroplets. Additionally, the cationic Dox was able to exploit electrostatic interactions with the carboxyl groups of PGA, further stabilizing the encapsulation. The successful encapsulation of the drug was confirmed by the extinction spectrum of the purified Dox-loaded NGs (NGs Dox) reported in Fig. S2,† which shows the absorption peak typical of Dox. The same UV-Vis spectrum was used to quantify the Dox content in the NGs by considering the absorbance at 480 nm, calibrated by using solutions of the free drug at different concentrations (see the calibration curve in Fig. S3†). Importantly, we did not observe significant differences in the Dox absorption spectra in free and encapsulated states, confirming that the encapsulation process did not alter the drug properties. The encapsulation efficiency (EE%) and drug loading (DL%) were estimated to be approximately 50% and 1.6% respectively, which is consistent with previous studies reporting Dox encapsulation in NGs.[34] The Dox-loaded NGs were then characterized and compared to their respective empty particles (Fig. 2, panels C and D). In terms of size, the empty nanoparticles (NGs Blank) had a hydrodynamic diameter of around 125 nm, while the Dox-loaded particles (NGs Dox) exhibited a diameter of approximately 135 nm. Both formulations displayed a low PDI, with values of 0.1 and 0.05, respectively. Zeta potential analysis revealed a value of −37.1 mV for the NGs Blank, with a slight increase to −30.9 mV in the NGs Dox, which is consistent with the positively charged Dox molecules (Fig. 2D). To gain a more detailed overview of the surface topology and morphology of the formulation, we performed SEM imaging of the NGs Blank (Fig. 3). Although the dried NGs tended to coalesce and cover the metallic sample holder surface, and the electron beam caused further fusion, the analysis of the aggregated NGs farther from the metallic surface (examples shown in Fig. 3) confirmed the spherical shape of the nanoparticles and a size on the order of a hundred nanometers.
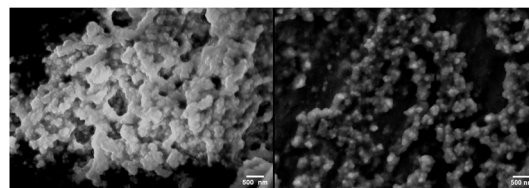


**Fig. 3** Representative SEM images of empty NGs spread over an aluminum surface. Scale bars: 500 nm.

In order to assess the long-term viability of the formulations, we measured the changes in size and PDI of the NGs over time to test their stability in PBS and DMEM (with 10% FBS) at 4 °C and −20 °C (Fig. 4). Both the empty and Dox-loaded NGs demonstrated good stability when stored at −20 °C for up to one month, showing no significant changes in size or PDI. The NGs Dox stored at 4 °C in PBS 1× showed the highest stability, maintaining their characteristics over more than two weeks. On the other hand, the empty NGs stored at 4 °C exhibited a slight increase in PDI (from 0.1 to 0.2) and a decrease in particle diameter and counts over a 15-day period. This behavior was more pronounced when the NGs Blank were stored in DMEM (10% FBS) at 4 °C, where a significant PDI increase and broadening of the distribution were observed in the first days (Fig. 4B). This was in stark contrast to the stability data of the same particles loaded with doxorubicin in the same medium over the duration of the experiment: these showed some minor changes but maintained appropriate sizes and PDIs. We can speculate that the pronounced instability of empty NGs in the considered cell medium might stem from the presence of FBS in the DMEM, which, although heat-inactivated, could still play a role in the disassembly of the particles. This phenomenon, however, does not occur with NGs Dox, likely due to the electrostatic interaction between Dox and the polymer enhancing the stability of the NGs, making them more resistant to degradation and/or aggregation under various storage conditions and in biological media.[35] This enhanced stability could arise also by possible different surface charge distribution and conformational changes within the nanogel network caused by the electrostatic interactions. In empty NGs, the carboxyl (–COOH) groups of PGA are predominantly deprotonated (–COO⁻) and tend to be exposed on the particle surface, conferring a highly negative zeta potential (−37.1 mV) that favors adsorption of positively charged serum proteins, leading to aggregation and increased PDI. Moreover, the polymer chains in empty NGs are highly hydrophilic and flexible, remaining exposed to the aqueous environment. In DMEM with FBS, interactions with serum proteins and ions induce cyclic swelling and dehydration of the network, increasing dimensional heterogeneity (PDI).[36] Upon Dox loading, the –COO⁻ groups become partially neutralized and are likely to be more oriented towards the interior of the nanogel due to interactions with the cationic drug. The resulting increased rigidity limits the possible conformational rearrangements triggered by serum proteins, thereby stabilizing the size distribution. These combined effects of altered surface charge and polymer conformation contribute
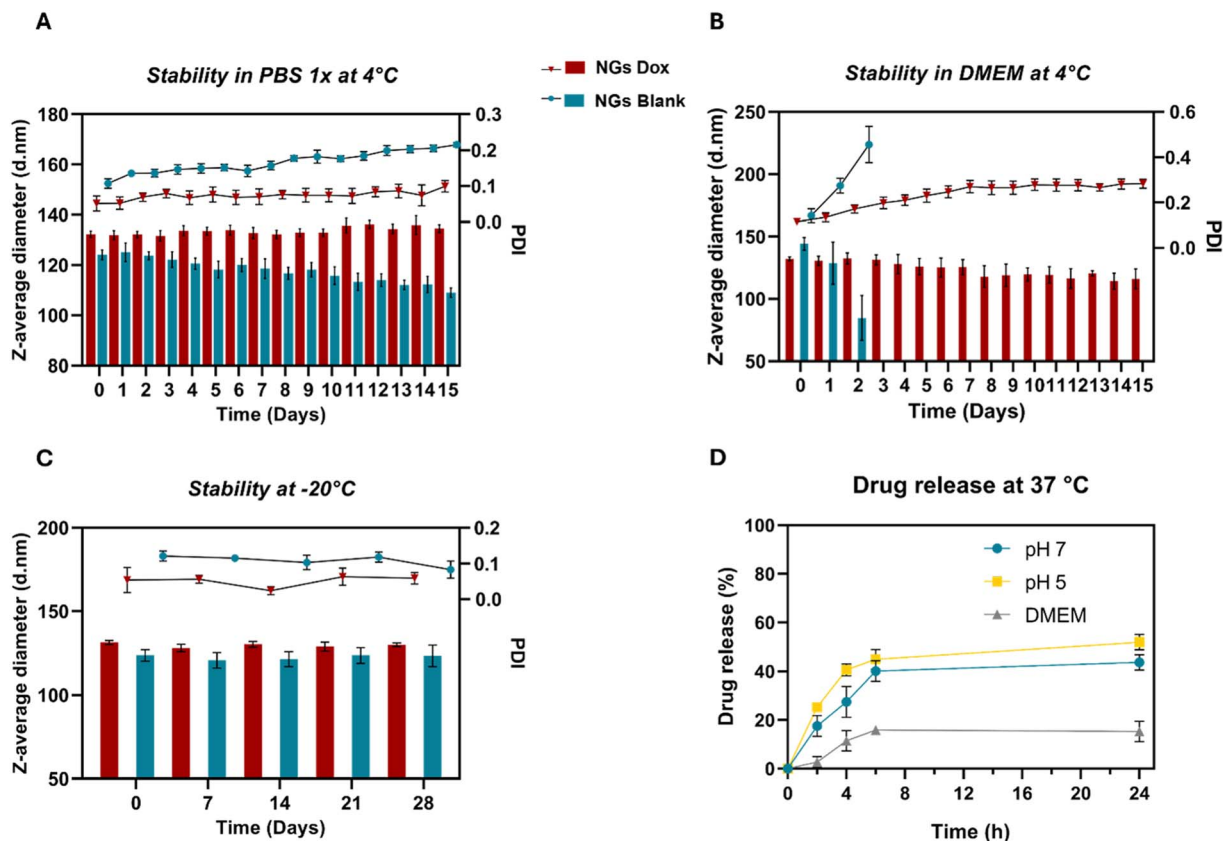
Fig. 4 *In vitro* stability of the empty and Dox-loaded NGs (NGs Blank and NGs Dox, respectively). (A–C) Behavior with time of the *Z*-average size (bars) and of the PDI (dots) for NGs Dox (in red) and NGs Blank (in blue), when stored at 4 °C in PBS 1× (A), at 4 °C in DMEM + 10% FBS (B) and at −20 °C in PBS 1× (C). Data are represented as average ± SD of three measurements taken from each of three different particle batches. (D) Drug release kinetics of NGs Dox under different conditions at various time points, using PBS 1× for pH 7 (blue dots and line), 100 mM acetate buffer for pH 5 (yellow squares and line), and complete DMEM with 10% FBS (gray triangles and line). Data presented as average ± SEM from $n = 3$ independent experiments.

to the superior stability of Dox-loaded NGs observed in DMEM with 10% FBS at 4 °C.

### NGs Dox drug release and cell internalization

We analyzed the drug release from the NGs *in vitro* under three different conditions at 37 °C, simulating physiological conditions with PBS 1× (pH 7), lysosomal conditions with 100 mM acetate buffer (pH 5), and a more complex environment, *i.e.* complete DMEM with FBS. The graph reported in Fig. 4D shows that particles at pH 5 and 7 have similar release patterns. A drug release peak was observed within the first 6 hours, followed by a plateau at 24 hours, with drug release remaining below 50–55% under all conditions. In contrast, in DMEM + 10% FBS, the maximum drug release was below 20%. We suppose that this behavior is due to the presence of FBS in the cell medium, which promotes the formation of a protein corona enhancing the structural stability of the NGs and hindering drug release. Previous studies have indeed noted altered drug release profiles from NGs due to the protein corona formation, suggesting potential differences between *in vitro* and *in vivo* release profiles.[37,38] In fact, drug release from NGs is mediated by multiple mechanisms, such as diffusion, structural

degradation, and possibly external triggers, especially *in vivo*; all these processes can depend on the environment.[39] In particular, when considering structures that interact with biological systems, it is essential to account for various forms of internalization into cells, such as uptake through the membrane, endocytosis, and other cellular processes.[40] The polymer used in this synthesis, PGA, is widely known for its biodegradability and biocompatibility. Within the body, lysosomal enzymes and proteases, such as cathepsin B, are responsible for the degradation of the PGA polymer chains, as extensively studied *in vitro*, and can trigger the release of the drug at the site of action, such as in tumor environments or within cells.[6,16] It is important to note that the evaluation reported in Fig. 4D does not account for these biological phenomena, focusing instead on diffusional effects, which, as previously described, are limited by the electrostatic interactions between the drug and the polymer. For the reasons discussed above, we investigated the cellular internalization of the NGs and of the drug. Typically, PGA nanogels with sizes comparable to our NGs undergo endocytic internalization mechanisms.[41,42] To explore the internalization pathways and cellular fate of our particles, we performed confocal microscopy analyses on live HeLa cells, exploiting the natural fluorescence

of Dox. We observed a marked difference in the internalization mechanisms between the doxorubicin-loaded NGs and the free drug. Fig. 5 shows that the free drug was present in the nucleus, as expected for a DNA intercalator, immediately after washing the cells after 30 minutes of incubation with Dox (time point 0 h), consistent with diffusion through membranes and into the cell. After one hour, the concentration of Dox in the nuclei (and the fluorescence from the cytoplasm) increased slightly (Fig. 5, 1 h), but no appreciable changes were observed at later time points, except for sustained cell death. However, we observed slower drug internalization upon administration of NGs Dox, suggesting a slower release from the nanoparticles probably undergoing a transport mediated by vesicles. Indeed, Fig. 6 shows that in the first half an hour after administration of NGs Dox (0 h, after cells washing) no Dox is present inside the nuclei, while there is a predominantly punctate fluorescence in the cytoplasm. Even if this fluorescence could also arise from autofluorescence from the cells, as shown in the control images taken from cells that did not receive any drug (Fig. 5, Ctrl), in this case the fluorescence seems higher and also partially diffuse within the cytoplasm. The rows labeled 1 h and 3 h in

Fig. 6 clearly show that the fluorescence intensity within the cells, particularly in their nuclei, steadily increases over time and continues to do so for at least up to three hours, even after washing the cells after 30 minutes from NGs Dox administration. This behavior indicates that the drug is released slowly, most probably due to the rupture of the NGs inside the cells, even if we cannot exclude some drug release into the medium from unwashed NGs adhering to cell membranes or to the glass, followed by diffusion into the cells and their nuclei. To investigate the internalization process further, we conducted experiments using NGs labeled with Alexa Fluor 647 bound to the polymer and encapsulating doxorubicin (NGs-D-647). To reach a recordable signal for the NGs-D-647, we used high excitation intensities and detector voltages. Some representative images are shown in Fig. S4† (Dox channel in red and Alexa Fluor 647 channel in green), where we report images taken from treated cells in the top row, and from control cells that did not receive any drug nor NGs in the bottom row. With this setup, we observed a detectable signal outside cells in the Alexa Fluor 647 channel, also for untreated control cells; most probably this is due to medium autofluorescence[43] (or to unwashed PGA-647
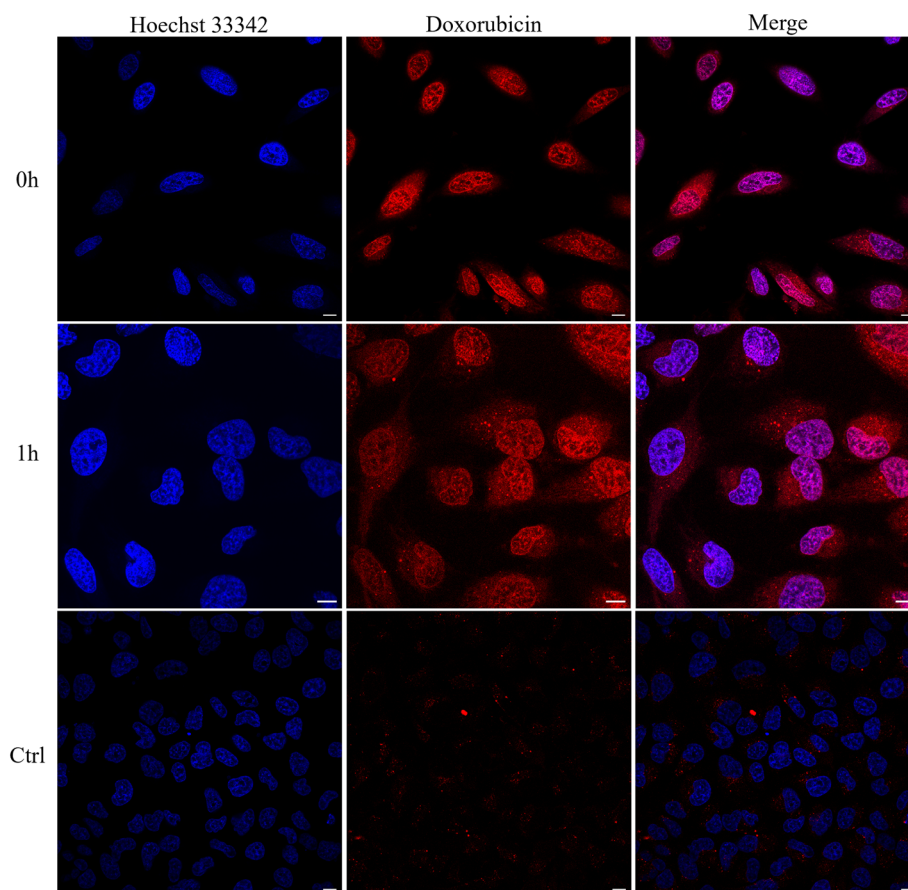


**Fig. 5** Confocal microscopy images of HeLa cells showing the time-dependent intracellular distribution of administered free doxorubicin, compared with control cells. In blue, the Hoechst 33342 channel (excitation 405 nm, emission band 430−470 nm) highlighting the nuclei; in red, the Dox channel (excitation 488 nm, emission band 570−620 nm). At 0 hours (top), corresponding to the time immediately after washing the cells, doxorubicin is already visible in the nuclei. After 1 hour (bottom), the drug diffused extensively throughout the cell, indicating rapid uptake and nuclear accumulation. Control cells (Ctrl), subjected to identical incubation conditions but without NGs or Dox, were analyzed to assess autofluorescence. Scale bar: 10 μm.
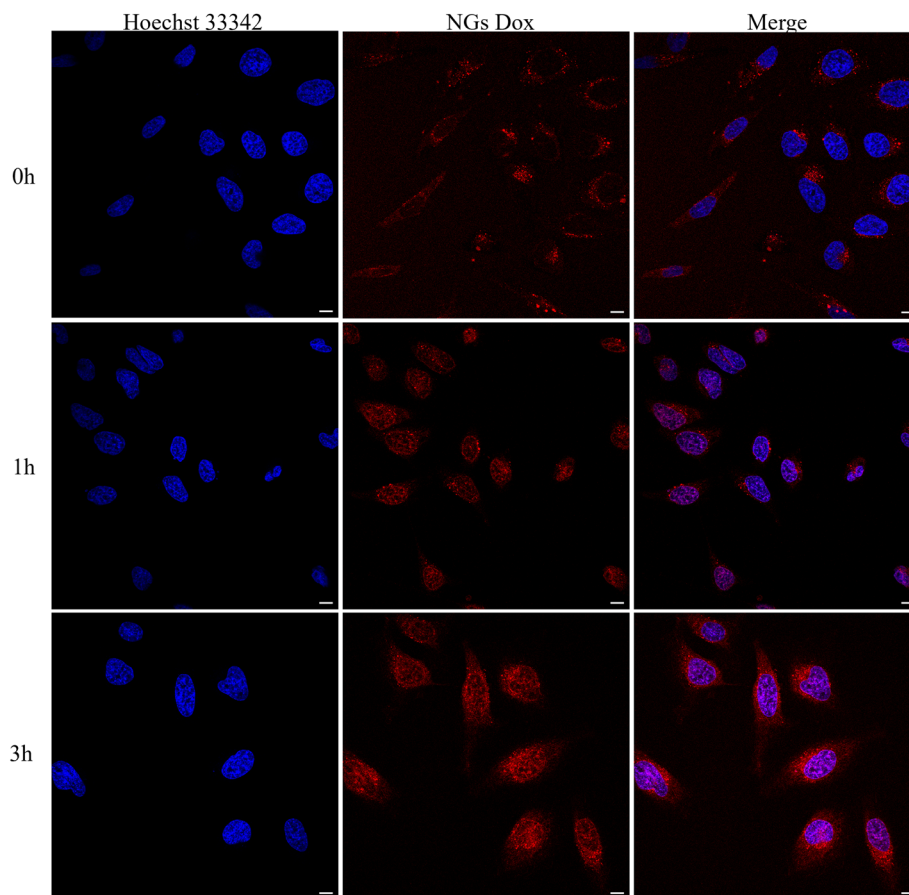
**Fig. 6** Confocal microscopy images of HeLa cells showing time–dependent uptake of Dox–loaded nanogels (NGs Dox); in blue, the Hoechst 33342 channel (excitation at 405 nm; emission band at 430–470 nm) highlighting the nuclei; in red, the Dox channel (excitation at 488 nm; emission band at 570–620 nm). At 0 hours (top), representing the time immediately after washing the cells, no significant accumulation of Dox in the nuclei is observed. After 1 hour (middle), Dox begins to accumulate in the nuclei. By 3 hours (bottom), fluorescence becomes more diffuse throughout the cells and much stronger in the nuclei, indicating effective intracellular delivery. Scale bar: 10 μm.

fluorescence for the top row), maybe with some stray-light reflection/diffusion component. We also detected dotted fluorescence from the cytoplasm of cells in both channels, most probably originating from vesicles, likely due to intrinsic metabolic activity or to natural fluorophores like the porphyrins in both samples (especially in the control),[44] but also from Dox and from PGA-647 in cells administered with NGs-D-647. However, only in this last case we observed colocalization between the two channels (top row of Fig. S4,† acquired 3 hours after half-an-hour incubation with NGs-D-647 and washing). Colocalization occurred in spots localized in the cytoplasm, often in perinuclear regions, likely corresponding to lysosomal vesicles. Minimal, if any, colocalization of the two signals occurred in the controls. This strongly suggests the presence of the NGs within internalization vesicles, and therefore an active internalization mediated by them, highlighting their ability to target and penetrate cells efficiently.

### *In vitro* cell viability

The *in vitro* cytotoxic effect of the NGs Dox was evaluated in HeLa cells over a 72-hour period using the MTS assay, and the results were compared with the ones obtained using the free drug at the same equivalent concentration. Empty nanogels (NGs) were also tested at an equivalent polymer concentration to that of the NGs Dox, ensuring the absence of cytotoxicity from the unloaded nanogels at the tested concentrations (Fig. S5†). The results reported in Fig. 7 show that the cytotoxic activity of the NGs Dox is similar to that of the free drug after 24, 48 and 72 hours of incubation. In particular, the 48-hour IC50 values were 2 μM and 1.64 μM for NGs Dox and free drug, respectively. Notably, the nanogel formulation demonstrated effective activity at as early as 24 hours, with performance comparable to that of the free drug. Although the 24-h viability is somehow higher for the NGs Dox at the highest tested concentrations (2 and 4 μM), it does not reproduce the one of a ≲20% drug concentration (expected from the data of Fig. 4D), indicating that the intracellular release (observed in Fig. 6) is more extensive. Moreover, the similar cytotoxic activity of the NGs and of the free drug at 48 and above all at 72 hours demonstrates sustained efficacy over time of the NGs Dox formulation. These findings, together with the confocal microscopy data, demonstrate a longer internalization time required by the NGs
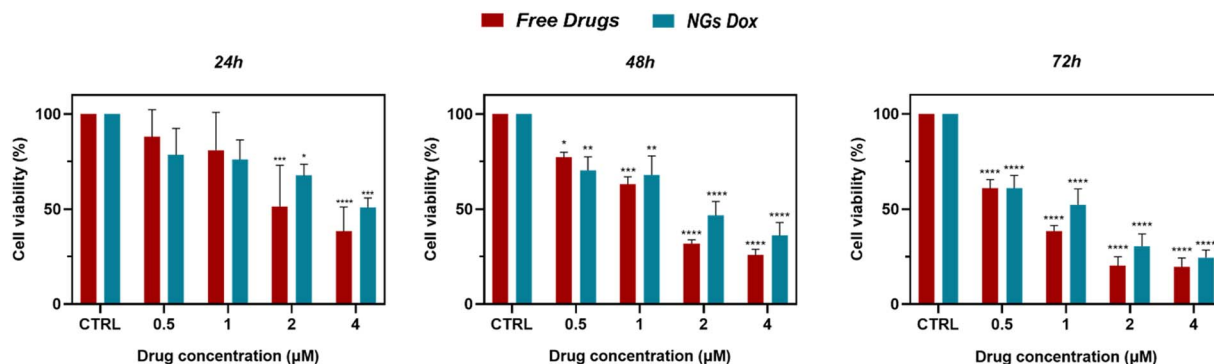
**Fig. 7** Evaluation of the cytotoxicity of doxorubicin and its NGs formulation using the MTS assay on HeLa cell cultures. $n = 3$, data presented as average $\pm$ SEM. Two-way ANOVA with Bonferroni post hoc test was used for comparisons against untreated control cells (CTRL). $*P < 0.05$, $**P < 0.01$, $***P < 0.001$, and $****P < 0.0001$, not significant is not indicated.

Dox, on the time scale of hours, but a comparable cellular cytotoxic effect at longer times, when compared to the free drug. If we consider the potential of the NGs as drug delivery systems, while their long-term effectiveness on cells is similar, it is important to note that the NGs and the free drug will have different bioavailability profiles and internalization processes *in vivo* (*e.g.*, administered by intravenous injection). While the free drug will permeate most cells and/or be excreted in a short time, the nanogel structure helps to protect the drug, gradually releasing it while preventing premature degradation or clearance, ensuring therefore its long-term availability. This capability allows for targeted accumulation at specific sites, primarily through the Enhanced Permeability and Retention (EPR) effect,[45] which is particularly beneficial in solid tumors. These properties are at the basis of the potential of nanogels as controlled, site-specific drug delivery systems, improving drug therapeutic efficacy while reducing off-target effects.

## Conclusions

In this work, we present the design and fabrication of an innovative nanostructured system based on chemically cross-linked PGA NGs, which could serve as an effective platform for drug delivery. The copper-free click-chemistry approach, combined with inverse nanoprecipitation, enables the rapid, clean, and straightforward production of nanoparticles while ensuring precise control over size and polydispersity index (PDI). Indeed, in the broader context of nanogel synthesis, two main strategies are typically employed: physical and chemical crosslinking. However, how mentioned in the introduction, physically crosslinked nanogels often present poor stability, especially upon dilution or medium exchange, and with them it is difficult to tune drug release under physiological conditions.[4,7] On the other side, the production of chemically cross-linked nanogels usually require toxic initiators, metal catalysts (like copper in the click-reaction CuAAC), or harsh synthesis conditions, and these can spoil encapsulated drugs or reduce biocompatibility.[8] The strategy presented here, based on SPAAC click chemistry, offers a valuable alternative: it ensures fast and highly efficient crosslinking under mild, metal-free, and fully aqueous conditions. Combined with inverse nanoprecipitation, this approach allows the formation of well-defined nanogels without the need for surfactants, catalysts, or initiators, enhancing both safety and reproducibility.

The system was extensively characterized: the NGs were spherical with a diameter of around 130 nm; they effectively encapsulated doxorubicin, and only partially released the drug in aqueous buffers and even less in a complete cell medium, over a timescale of some hours. The use of doxorubicin as a model chemotherapeutic agent points out also the potential application of this system in drug delivery. Our confocal microscopy analyses highlight that these nanogels effectively interact with and are internalized by cancer cells, protecting the drug in the first hour(s) but releasing it in two/three hours. The cytotoxicity assays further confirmed that the NGs Dox formulation can deliver the drug efficiently, achieving a performance comparable to that of the free drug at equivalent concentrations. The developed NGs, thanks to their small size and to the characteristics of the polymer, have the potential to be used as controlled drug delivery system; future modifications could further improve their specificity by incorporating targeting moieties (aptamers, antibodies, *etc.*)[46,47] capable of recognizing and binding to specific molecules on the cell membrane, particularly those with accessible extracellular domains.[48] Moreover, the versatility of this system suggests an even broader applicability: given its rapid and simple synthesis process, excellent stability, and tunable properties, it could also be employed for the delivery of other therapeutic molecules, such as proteins or peptides. Overall, these results provide a solid foundation for further optimization and development of this platform as a promising tool for advanced drug delivery and precision medicine applications.

## Experimental section

### Materials

All chemicals were reagent grade, obtained from Sigma-Aldrich, and used without further purification unless otherwise indicated. Poly(L-glutamic acid sodium salt) (PGA) MW = 15 000–50 000 was purchased from Sigma-Aldrich. Poly(L-glutamic acid

sodium salt) graft azide (PGA–N$_3$) MW = 34 000 Da, 10% side chain functionalization, was purchased from Alamanda Polymers, Inc. (AL, Huntsville, USA). Dibenzocyclooctyne–amine (DBCO–NH$_2$) was purchased from MedChemExpress (NJ, USA). $N$-(3-Dimethylaminopropyl)-$N'$-ethylcarbodiimide (EDC) was purchased from Sigma-Aldrich. Doxorubicin hydrochloride (Dox·HCl) was purchased from MedChemExpress (NJ, USA). Dulbecco's Modified Eagle's Medium (DMEM) high glucose, phosphate buffer saline (PBS), fetal bovine serum (FBS), and trypsin were purchased from Gibco. 3-(4,5-Dimethylthiazol-2-yl)-5-(3-carboxymethoxyphenyl)-2-(4-sulfophenyl)-2$H$-tetrazolium (MTS) was supplied by Promega (Spain). All solvents were of analytical grade and were used as received. Ultrapure water was used for all aqueous preparations (Milli-Q, Millipore). Nanogel purification was performed using MicroSpin G-50 columns (GE Healthcare) and 0.45 μm nylon membrane centrifugal filters (VWR®), following the manufacturer's instructions.

### Synthesis of DBCO-derivatized PGA precursors

100 μL of PGA with molecular weight 15–50 kDa was prepared at 10 mg mL$^{-1}$ using 2-($N$-morpholino)ethane-sulfonic acid (MES) buffered saline (MBS) at pH 6.5. EDC was added at a 1.5-fold molar excess relative to glutamate monomers and the reaction was allowed to proceed for 20 minutes at room temperature under gentle agitation. DBCO–NH$_2$ was dissolved in DMSO at a concentration of 70 mg mL$^{-1}$ and added to the reaction. Upon optimization of reaction conditions, varying amounts of DBCO–NH$_2$ were used to achieve different degrees of functionalization: a 14 mol% feed of DBCO–NH$_2$ (relative to glutamate monomers) resulted in 10% substitution, while a 30 mol% feed (relative to glutamate monomers) yielded 20% substitution. The reaction was maintained at room temperature with agitation for 4 hours. To remove unreacted DBCO–NH$_2$, the activated polymer (PGA–DBCO) was passed through a 10 kDa MWCO Amicon® Ultra Centrifugal Filter (at 8000 × $g$ for 10 min, room temperature) and washed 3 to 5 times with ultrapure water. To verify the conjugation, the reaction mixture was injected into an HPLC system (Dionex Ultra 3000) equipped with a PolySep-GFC-P 4000 LC Column (300 × 7.8 mm) and a PolySep-GFC-P Guard Column (35 × 7.8 mm) (Phenomenex Inc., Italy), with phosphate-buffered saline (1×, pH 7.4) as the mobile phase. The degree of DBCO coupling to the polymer was estimated by measuring the concentration of DBCO via UV-Vis spectroscopy at an absorbance of 310 nm.

### Synthesis of fluorophore-labeled PGA

3 mg of EDC and 50 nmol of ATTO 647 cadaverine (Thermo Fisher Scientific) was added to a 100 μL solution of 10 mg mL$^{-1}$ of PGA–N$_3$ in PBS 1×. The mixture was stirred for 24 hours at room temperature, and the final product was purified using a 10 kDa MWCO Amicon® Ultra Centrifugal Filter (at 8000 × $g$ for 10 minutes, room temperature) three times with water or until a clear eluate was obtained. The resulting labeled PGA (PGA-647) was stored at −20 °C until use. The reaction mixture was analyzed to confirm the conjugation using an HPLC system

(Dionex Ultra 3000) equipped with a PolySep-GFC-P 4000 LC column (300 × 7.8 mm) and a PolySep-GFC-P Guard column (35 × 7.8 mm) (Phenomenex Inc., Italy), employing phosphate-buffered saline (1×, pH 7.4) as the mobile phase. Conjugation success was confirmed by detecting absorbance at 647 nm; the whole spectrum, reported in Fig. S6,† was measured using an Agilent Technologies Cary 3500 UV-Vis spectrophotometer and a 1 cm quartz cuvette.

### Optimization of the synthesis and preparation of PGA-based NGs

Several reaction parameters were evaluated to identify the optimal SPAAC conditions for the coupling of PGA–N$_3$ and PGA–DBCO precursors directly within an inverse nanoprecipitation setup, leading to the formation of PGA-based NGs. PGA–N$_3$ (10% substitution) and PGA–DBCO (substitution 10% or 20%) were dissolved in water at a concentration of 10 mg mL$^{-1}$. The two solutions were mixed in the ratios shown in Table 1, with a final volume of 100 μL. The aqueous solution was then dripped into acetone under agitation using a thermomixer (25 °C, 800 rpm). After 5 minutes, the velocity of the thermomixer was reduced to 500 rpm, and the solution was left to react in a closed 2 mL Eppendorf tube for 5 hours or overnight (see also below). The organic solvent was then evaporated using a dry nitrogen flux. The resulting NG solution was purified using a MicroSpin G-50 column and resuspended in phosphate-buffered saline (PBS) buffer at a concentration of 1×. Finally, the resulting NGs were either freeze-dried or stored in solution at 4 °C. This approach enabled optimization of the coupling reaction under conditions specifically tailored to achieve the desired hydrodynamic radius and PDI for the NGs, allowing for a time-efficient single-step process. Reactions were assessed at two time points, after 5 hours and overnight, to determine the effect of reaction time on the formation and properties of the NGs; the overnight reaction condition was chosen in the final implementation. Entry 6 of Table 1 presents the parameters selected as the standard for all subsequent experiments in this study. For the preparation of fluorescence-labeled NGs (NGs-D-647 and NGs-647) we used PGA-647 in place of standard PGA, following the same formulation protocol.

### Drug encapsulation

To produce NGs containing doxorubicin hydrochloride (Dox), the drug was dissolved in water and added to the polymer solution containing PGA–N$_3$ and PGA–DBCO described above, at a drug/polymer mass ratio of 1 : 50. This solution was used for the same protocol described previously. Direct methods were used to determine Dox encapsulation inside the NGs, as detailed below. After inverse nanoprecipitation, the organic solvent was evaporated and the product was filtered through a MicroSpin G-50 column. The purified product was then diluted in PBS 1× to a final volume of 200 μL. The concentration of the drug in this suspension was measured by ultraviolet-visible (UV-Vis) absorption spectroscopy at 480 nm using an Agilent Technologies Cary 3500 UV-Vis spectrophotometer and a 1 cm quartz cuvette, using a calibration curve prepared with

doxorubicin in ultrapure water. The calibration curve (Fig. S7†) was linear over the concentration range of 0.78 to 50 μg mL$^{-1}$. The drug encapsulation efficiency (EE%) and loading capacity (LC%) were calculated using the equations given below.

$$EE\ (\%) = \frac{\text{mass of drugs encapsulated}}{\text{total mass of drugs added}} \times 100$$

$$LC\ (\%) = \frac{\text{mass of drugs encapsulated}}{\text{mass of nanogel}} \times 100$$

### Physicochemical characterization

**Particle size distribution and morphology.** The particle size distribution (average diameter and polydispersity index) was analyzed by Dynamic Light Scattering (DLS) using a Malvern Zetasizer Nano ZS instrument with a 633 nm laser at a fixed scattering angle of 173°. NG solutions (5 mg mL$^{-1}$ in PBS 1×) were sonicated for 2 minutes, filtered through a 0.45 μm nylon membrane filter (VWR®), and then measured. For each compound, size distribution was determined in triplicate with five measurements per sample. The reported values, including the Z-average size and the polydispersity index (PDI) determined by cumulant analysis, represent the mean ± standard deviation (SD) calculated from at least three independent batches of nanoparticles. Automatic optimization of beam focusing and attenuation was applied to each measurement. The morphology of the nanospheres was ascertained using a Scanning Electron Microscope (SEM): samples were prepared by evaporating 2 μL drops of 0.5 mg mL$^{-1}$ of NGs Blank solution in 0.5× PBS directly onto an aluminum pin stub, which then inserted in the SEM. The microscopy analysis was performed using a field emission gun (FEG) SEM Merlin from ZEISS (Oberkochen, Germany); micrographs were captured at 5 kV, with a working distance (WD) of 3.2 mm and at magnifications ranging from 8000× to 16 000×; to reduce the charge accumulation the samples were fluxed with an N$_2$ gas injector system at 30% saturation.

**Zeta potential.** Nanoparticles were further characterized for zeta potential (ζ). Measurements were performed at 25 °C using a Malvern Zetasizer Nano ZS instrument with a 633 nm laser and disposable folded capillary cells (Malvern Instruments Ltd). NG solutions were prepared in 0.1× PBS at pH 7.4 and filtered through a 0.45 μm nylon membrane filter (VWR®). Zeta potential for each sample was measured in triplicate, with five measurements taken per sample. The net electrophoretic mobility (μ) was measured and converted to zeta potential (ζ), with data directly analyzed and processed using Malvern Zetasizer software (Version 7.13).

**Fourier-transform infrared spectroscopy (FT-IR).** Infrared spectra were acquired with a Cary 630 spectrometer (Agilent Technologies) using a single reflection ZnSe ATR module. The spectra were collected at room temperature with a resolution of 2 cm$^{-1}$ and averaging 256 individual scans for the spectral range included between 4000 and 650 cm$^{-1}$. All measurements were carried out on powders: PGA–DBCO and NG samples were

freeze-dried using a freeze-dryer Lyovapor L-200 from Büchi (Flawil, Swiss Confederation), while PGA–N$_3$ sodium salt was used as received in its original form.

**NMR spectroscopy.** The $^1$H NMR analysis was performed with a Bruker Avance III 300 spectrometer. Chemical shifts are given in parts per million (ppm), calibrated using the residual solvent peak of H$_2$O in deuterium oxide (D$_2$O). PGA–N$_3$ was used as supplied, while PGA–DBCO and the NGs were freeze-dried, prior to resuspension in D$_2$O. For the analysis, 10 mg of PGA–DBCO or PGA–N$_3$ were dissolved in 350 μL of D$_2$O, while an approximately equivalent amount of NPs was prepared in the same manner. All NMR spectra were acquired at a frequency of 300.130 MHz, in a spectral window of 20.0 ppm (6009.6 Hz) and with 65 536 scans.

**Nanogel stability.** To assess the stability of the NGs, the particles were stored under different conditions. For short-term stability, NGs were stored at 4 °C in PBS and cell culture medium (DMEM with 10% heated-inactivated FBS). The NGs stored at 4 °C were measured daily for up to 15 days. For long-term stability, NGs were stored at −20 °C in PBS supplemented with trehalose (1 mg mL$^{-1}$) as a cryoprotectant. These samples were divided into aliquots, with each aliquot thawed separately for the measurement, and the NGs were measured weekly for up to 4 weeks. The stability of the NGs was monitored by Dynamic Light Scattering (DLS) measurements, focusing on the hydrodynamic diameter and the polydispersity index (PDI). The results are presented as the means ± SD of the Z-average sizes and of the PDIs as determined by cumulants fit, from three independent experiments with five measurements per sample.

**In vitro drug release studies.** The in vitro release profiles of doxorubicin (Dox) from NGs Dox were analyzed under conditions simulating physiological and intracellular environments. 1 mg of Dox-loaded NGs were dissolved in acetate buffer (50 mM, pH 5.2), PBS (1×, pH 7.4), or cell culture medium (DMEM with 10% heat-inactivated FBS) and incubated at 37 °C with stirring at 600 rpm on a thermomixer. At specified intervals, aliquots were collected and passed through a Sephadex G50 column to separate free Dox from the NGs. Free Dox was retained in the resin, while the Dox-loaded NGs were collected, freeze-dried, re-dissolved in PBS 1× and analyzed by UV-Vis absorption spectroscopy (λ = 480 nm) to quantify the remaining Dox encapsulated in the NGs.

**Cell culture and biological procedures.** HeLa cells, a human cervical cancer cell line, were obtained from the American Type Culture Collection (ATCC, Manassas, VA, USA). Cells were cultured in adhesion in high glucose DMEM (Dulbecco's Modified Eagle Medium), supplemented with 10% heat-inactivated fetal bovine serum (FBS) (Gibco), 100 unit per mL of streptomycin, 100 units per mL of penicillin, 2 mM L-glutamine, and 1 mM sodium pyruvate (Gibco) at 37 °C in a humidified incubator with an atmosphere with 5% CO$_2$. Cells were maintained in an exponential growth phase, and the medium was replaced every 2–3 days. Cells underwent passage once weekly when 80% confluence was reached.

**Evaluation of cell viability via MTS assay.** The cells were seeded in sterile 96-well microtiter plates at a density of 20 000 cells per well in 100 μL of growth medium and incubated

overnight. After incubation, free drugs and drug-loaded NGs were added to the cells, after appropriate dilution of these formulations in the culture medium to achieve final concentrations ranging from 4 to 0.5 mM of Dox. In parallel, cells were also incubated with different dilutions of drug-free NGs at the same concentration of the Dox-containing ones for the same time periods, to assess the possible cytotoxic effect of the polymer used to prepare the nanoparticles. The cells were incubated with these formulations for 24, 48, and 72 hours. Following incubation, 10 μL of MTS solution (Promega) was added to each well, and the cells were incubated for an additional 3 hours. The optical density was measured at 490 nm using a Tecan Infinite® 200 PRO plate reader. Cell viability was expressed as a percentage of the absorbance with respect to the one of the untreated control cells after subtracting the background signal from a well containing only the cell culture medium.

**Live-cell imaging using confocal fluorescence microscopy.** For live-cell imaging, HeLa cells were plated at a density of $5 \times 10^4$ cells per well in 35 mm glass-bottom culture dishes (Ibidi GmbH) and incubated for 24 hours at 37 °C with 5% $CO_2$. Dox-loaded NGs with a final equivalent concentration of 2.5 μM Dox, or the same concentration of free Dox, were then added. After 30 minutes of incubation, the cells were washed with PBS and imaged immediately or maintained in fresh medium for various time intervals (15 minutes, 30 minutes, 1 hour, and 3 hours at 37 °C). The nuclear marker Hoechst 33342 (1 μL of a 5 mM solution) was added five minutes prior to washing the cells. The same protocol was applied for NGs-D-647 to investigate the colocalization of Dox with the NGs, and to understand the endocytic pathway. Imaging was performed using an OLYMPUS IX83 microscope equipped with a confocal Fluoview FV3000 system (Shinjuku, Tokyo, Japan), using a 60× oil immersion objective. Excitation wavelengths included 405 nm for Hoechst, 488 nm for Dox, and 647 nm for AlexaFluor, with emission bands of 430–470, 570–620, and 650–750, respectively. Different fluorescent channels were acquired sequentially per line, and the brightfield images were acquired simultaneously with the Dox Channel (488 nm excitation). Control cells subjected to identical incubation conditions but without NGs or Dox were analyzed to assess autofluorescence. Images were exported from Olympus FV315-SW software and processed using ImageJ.[49]

## Abbreviations

| | |
|---|---|
| NGs | Nanogels |
| Dox | Doxorubicin |
| PGA | Poly(α-glutamic acid) |
| SPAAC | Strain-promoted azide–alkyne cycloaddition |
| HPCL | High performance liquid chromatography |

## Data availability

All data supporting the findings of this article are included in the ESI† file submitted alongside the manuscript. No additional datasets, software, or code have been deposited in external repositories.

## Author contributions

P. M. developed the concept and design of the project, performed the synthesis and physicochemical characterization, conducted the drug-release profiles experiments, performed the cell work, prepared the figures and wrote the manuscript. A. M. conducted the NMR and FTIR experiments and contributed to the respective sections of the manuscript. A. G. conducted the SEM experiments, analyzed the SEM images, and contributed to the morphological characterization of the nanogels. S. L. contributed to the project design, supervised the experiments, contributed to some figures, and wrote and revised the manuscript. Analysis and interpretation of the data included contributions from all authors. All authors have given approval to the final version of the manuscript.

## Conflicts of interest

There are no conflicts to declare.

## References

1 P. Mastella, B. Todaro and S. Luin, Nanogels: Recent Advances in Synthesis and Biomedical Applications, *Nanomaterials*, 2024, **14**(15), 1300. Available from: **https://www.mdpi.com/2079-4991/14/15/1300**.

2 I. Altinbasak, Y. Alp, R. Sanyal and A. Sanyal, Theranostic nanogels: multifunctional agents for simultaneous therapeutic delivery and diagnostic imaging, *Nanoscale*, 2024, **16**(29), 14033–14056. Available from: **https://xlink.rsc.org/?DOI=D4NR01423E**.

3 M. A. Grimaudo, A. Concheiro and C. Alvarez-Lorenzo, Nanogels for regenerative medicine, *J. Controlled Release*, 2019, **313**, 148–160. Available from: **https://linkinghub.elsevier.com/retrieve/pii/S0168365919305553**.

4 A. G. Rusu, A. P. Chiriac, L. E. Nita, I. Rosca, D. Rusu and I. Neamtu, Self-Assembled Nanocarriers Based on Modified Chitosan for Biomedical Applications: Preparation and Characterization, *Polymers*, 2020, **12**(11), 2593. Available from: **https://www.mdpi.com/2073-4360/12/11/2593**.

5 S. Muñana-González, A. Veloso-Fernández, L. Ruiz-Rubio, L. Pérez-Álvarez and J. L. Vilas-Vilela, Covalent Cross-Linking as a Strategy to Prepare Water-Dispersible Chitosan Nanogels, *Polymers*, 2023, **15**(2), 434. Available from: **https://www.mdpi.com/2073-4360/15/2/434**.

6 A. Duro-Castano, A. Sousa-Herves, A. Armiñán, D. Charbonnier, J. J. Arroyo-Crespo, S. Wedepohl, *et al.*, Polyglutamic acid-based crosslinked doxorubicin nanogels as an anti-metastatic treatment for triple negative breast cancer, *J. Controlled Release*, 2021, **332**, 10–20. Available from: **https://linkinghub.elsevier.com/retrieve/pii/S0168365921000523**.

7 S. Shah, N. Rangaraj, K. Laxmikeshav and S. Sampathi, Nanogels as drug carriers – Introduction, chemical aspects,

release mechanisms and potential applications, *Int. J. Pharm.*, 2020, **581**, 119268. Available from: https://linkinghub.elsevier.com/retrieve/pii/S0378517320302520.

8 H. Y. Yoon, D. Lee, D. Lim, H. Koo and K. Kim, Copper-Free Click Chemistry: Applications in Drug Delivery, Cell Tracking, and Tissue Engineering, *Adv. Mater.*, 2022, **34**(10), 2107192. Available from: https://onlinelibrary.wiley.com/doi/10.1002/adma.202107192.

9 S. Chakroborty, N. Nath, A. Mahal, A. Barik, A. R. Panda, Fahaduddin, *et al.*, Stimuli-responsive nanogels: A smart material for biomedical applications, *J. Mol. Liq.*, 2024, **403**, 124828. Available from: https://linkinghub.elsevier.com/retrieve/pii/S0167732224008845.

10 N. Kumar, S. Singh, P. Sharma, B. Kumar and A. Kumar, Single-, Dual-, and Multi-Stimuli-Responsive Nanogels for Biomedical Applications, *Gels*, 2024, **10**(1), 61. Available from: https://www.mdpi.com/2310-2861/10/1/61.

11 A. J. Sivaram, P. Rajitha, S. Maya, R. Jayakumar and M. Sabitha, Nanogels for delivery, imaging and therapy, *WIREs Nanomedicine and Nanobiotechnology*, 2015, **7**(4), 509–533. Available from: https://wires.onlinelibrary.wiley.com/doi/10.1002/wnan.1328.

12 R. Kandil and O. M. Merkel, Recent progress of polymeric nanogels for gene delivery, *Curr. Opin. Colloid Interface Sci.*, 2019, **39**, 11–23. Available from: https://linkinghub.elsevier.com/retrieve/pii/S1359029418301146.

13 L. C. Johnson, A. T. Akinmola and C. Scholz, Poly(glutamic acid): From natto to drug delivery systems, *Biocatal. Agric. Biotechnol.*, 2022, **40**, 102292. Available from: https://linkinghub.elsevier.com/retrieve/pii/S1878818122000196.

14 W. E. Hanby, S. G. Waley and J. Watson, 632. Synthetic polypeptides. Part II. Polyglutamic acid, *J. Chem. Soc.*, 1950, 3239. Available from: https://xlink.rsc.org/?DOI=jr9500003239.

15 I. Shih, Y. Van and M. Shen, Biomedical Applications of Chemically and Microbiologically Synthesized Poly(Glutamic Acid) and Poly(Lysine), *Mini-Rev. Med. Chem.*, 2004, **4**(2), 179–188. Available from: http://www.eurekaselect.com/openurl/content.php?genre=article&issn=1389-5575&volume=4&issue=2&spage=179.

16 K. Fan, D. Gonzales and M. Sevoian, Hydrolytic and enzymatic degradation of poly(γ-glutamic acid) hydrogels and their application in slow-release systems for proteins, *J. Environ. Polym. Degrad.*, 1996, **4**(4), 253–260. Available from: http://link.springer.com/10.1007/BF02070694.

17 T. Sedlačík, H. Studenovská and F. Rypáček, Enzymatic degradation of the hydrogels based on synthetic poly(α-amino acid)s, *J. Mater. Sci.:Mater. Med.*, 2011, **22**(4), 781–788. Available from: http://link.springer.com/10.1007/s10856-011-4275-x.

18 I. Ekladious, Y. L. Colson and M. W. Grinstaff, Polymer–drug conjugate therapeutics: advances, insights and prospects, *Nat. Rev. Drug Discovery*, 2019, **18**(4), 273–294. Available from: https://www.nature.com/articles/s41573-018-0005-0.

19 C. E. Markwalter, R. F. Pagels, A. N. Hejazi, A. G. R. Gordon, A. L. Thompson and R. K. Prud'homme, Polymeric Nanocarrier Formulations of Biologics Using Inverse Flash NanoPrecipitation, *AAPS J.*, 2020, **22**(2), 18. Available from: http://link.springer.com/10.1208/s12248-019-0405-z.

20 E. Anooj, M. Charumathy, V. Sharma, B. V. Vibala, S. T. Gopukumar, S. I. B. Jainab, *et al.*, Nanogels: An overview of properties, biomedical applications, future research trends and developments, *J. Mol. Struct.*, 2021, **1239**, 130446. Available from: https://linkinghub.elsevier.com/retrieve/pii/S0022286021005792.

21 K. Öztürk, M. Kaplan and S. Çalış, Effects of nanoparticle size, shape, and zeta potential on drug delivery, *Int. J. Pharm.*, 2024, **666**, 124799. Available from: https://linkinghub.elsevier.com/retrieve/pii/S0378517324010330.

22 Y. Li, D. Maciel, J. Rodrigues, X. Shi and H. Tomás, Biodegradable Polymer Nanogels for Drug/Nucleic Acid Delivery, *Chem. Rev.*, 2015, **115**(16), 8564–8608. Available from: https://pubs.acs.org/doi/10.1021/cr500131f.

23 J. É. F. Radu, L. Novak, J. F. Hartmann, N. Beheshti, A. L. Kjøniksen, B. Nyström, *et al.*, Structural and dynamical characterization of poly-gamma-glutamic acid-based cross-linked nanoparticles, *Colloid Polym. Sci.*, 2008, **286**(4), 365–376.

24 I. Kwiecień, D. Niewolik, A. I. Ekere, A. Gupta and I. Radecka, Synthesis of hydrogels made of poly-γ-glutamic acid (γ-PGA) for potential applications as probiotic-delivery vehicles, *Appl. Sci.*, 2020, **10**(8), 2787.

25 A. M. Castillo, L. Patiny and J. Wist, Fast and accurate algorithm for the simulation of NMR spectra of large spin systems, *J. Magn. Reson.*, 2011, **209**(2), 123–130.

26 A. M. Castillo, L. Patiny and J. Wist, *Predict $^1$H Proton NMR Spectra*, 2015, available from: https://www.nmrdb.org/new_predictor/index.shtml?v=v2.157.0, [Accessed 2025-07-02].

27 R. C. Cooper, J. Wang and H. Yang, Injectable Dendrimer Hydrogel Delivers Melphalan in Both Conjugated and Free Forms for Retinoblastoma, *Biomacromolecules*, 2024, **25**(9), 5928–5937.

28 J. Qiao, F. Tian, Y. Deng, Y. Shang, S. Chen, E. Chang, *et al.*, Bio-orthogonal click-targeting nanocomposites for chemo-photothermal synergistic therapy in breast cancer, *Theranostics*, 2020, **10**(12), 5305–5321.

29 P. Gobbo, Z. Mossman, A. Nazemi, A. Niaux, M. C. Biesinger, E. R. Gillies, *et al.*, Versatile strained alkyne modified water-soluble AuNPs for interfacial strain promoted azide-alkyne cycloaddition (I-SPAAC), *J. Mater. Chem. B*, 2014, **2**(13), 1764–1769.

30 A. Ramazani, F. Z. Nasrabadi, A. Rezaei, M. Rouhani, H. Ahankar, P. A. Asiabi, *et al.*, Synthesis of N-acylurea derivatives from carboxylic acids and N,N′-dialkyl carbodiimides in water, *J. Chem. Sci.*, 2015, **127**(12), 2269–2282.

31 A. Karayel, S. Özbey, C. Kuş and G. Ayhan-Kılcıgil, Restricted rotation around the methylene bridge of 5-(2-p-(chlorophenyl)benzimidazol-1-yl)methyl-4-(o-substitutedphenyl)-2,4-dihydro-[1,2,4]-triazole-3-thiones as evidenced by NMR, X-RAY and DFT studies and the importance of low energy rotational conform, *J. Mol. Struct.*, 2019, **1177**, 476–484.

32 V. Taresco, J. Suksiriworapong, R. Creasey, J. C. Burley, G. Mantovani, C. Alexander, *et al.*, Properties of acyl modified poly(glycerol-adipate) comb-like polymers and their self-assembly into nanoparticles, *J. Polym. Sci., Part A:Polym. Chem.*, 2016, **54**(20), 3267–3278.

33 M. Kciuk, A. Gielecińska, S. Mujwar, D. Kołat, Ż. Kałuzińska-Kołat, I. Celik, *et al.*, Doxorubicin—An Agent with Multiple Mechanisms of Anticancer Activity, *Cells*, 2023, **12**(4), 659. Available from: https://www.mdpi.com/2073-4409/12/4/659.

34 M. Li, W. Song, Z. Tang, S. Lv, L. Lin, H. Sun, *et al.*, Nanoscaled Poly(L-glutamic acid)/Doxorubicin-Amphiphile Complex as pH-responsive Drug Delivery System for Effective Treatment of Nonsmall Cell Lung Cancer, *ACS Appl. Mater. Interfaces*, 2013, **5**(5), 1781–1792. Available from: https://pubs.acs.org/doi/10.1021/am303073u.

35 M. Mohammadi, L. Arabi and M. Alibolandi, Doxorubicin-loaded composite nanogels for cancer treatment, *J. Controlled Release*, 2020, **328**, 171–191. Available from: https://linkinghub.elsevier.com/retrieve/pii/S0168365920304740.

36 K. Strojan, A. Leonardi, V. B. Bregar, I. Križaj, J. Svete and M. Pavlin, Dispersion of Nanoparticles in Different Media Importantly Determines the Composition of Their Protein Corona, *PLoS One*, 2017, **12**(1), e0169552. Available from: https://dx.plos.org/10.1371/journal.pone.0169552.

37 S. Behzadi, V. Serpooshan, R. Sakhtianchi, B. Müller, K. Landfester, D. Crespy, *et al.*, Protein corona change the drug release profile of nanocarriers: The "overlooked" factor at the nanobio interface, *Colloids Surf., B*, 2014, **123**, 143–149. Available from: https://linkinghub.elsevier.com/retrieve/pii/S0927776514004779.

38 K. Obst, G. Yealland, B. Balzus, E. Miceli, M. Dimde, C. Weise, *et al.*, Protein Corona Formation on Colloidal Polymeric Nanoparticles and Polymeric Nanogels: Impact on Cellular Uptake, Toxicity, Immunogenicity, and Drug Release Properties, *Biomacromolecules*, 2017, **18**(6), 1762–1771. Available from: https://pubs.acs.org/doi/10.1021/acs.biomac.7b00158.

39 G. H. Son, B. J. Lee and C. W. Cho, Mechanisms of drug release from advanced drug formulations such as polymeric-based drug-delivery systems and lipid nanoparticles, *J. Pharm. Invest.*, 2017, **47**(4), 287–296.

40 F. Toscano and M. Torres-Arias, Nanoparticles cellular uptake, trafficking, activation, toxicity and in vitro evaluation, *Curr. Res. Immunol.*, 2023, **4**, 100073. Available from: https://linkinghub.elsevier.com/retrieve/pii/S2590255523000197.

41 J. J. Rennick, A. P. R. Johnston and R. G. Parton, Key principles and methods for studying the endocytosis of biological and nanoparticle therapeutics, *Nat. Nanotechnol.*, 2021, **16**(3), 266–276. Available from: https://www.nature.com/articles/s41565-021-00858-8.

42 S. F. Peng, M. T. Tseng, Y. C. Ho, M. C. Wei, Z. X. Liao and H. W. Sung, Mechanisms of cellular uptake and intracellular trafficking with chitosan/DNA/poly(γ-glutamic acid) complexes as a gene delivery vector, *Biomaterials*, 2011, **32**(1), 239–248.

43 C. Schirripa Spagnolo, C. Spagnolo, A. Moscardini, R. Amodeo, F. Beltram and S. Luin, Optimized Two-Color Single-Molecule Tracking of Fast-Diffusing Membrane Receptors, *Adv. Opt. Mater.*, 2024, **12**(9), 2302012.

44 R. Teixeira, V. V. Serra, D. Botequim, P. M. R. Paulo, S. M. Andrade and S. M. B. Costa, Fluorescence Spectroscopy of Porphyrins and Phthalocyanines: Some Insights into Supramolecular Self-Assembly, Microencapsulation, and Imaging Microscopy, *Molecules*, 2021, **26**(14), 4264. Available from: https://www.mdpi.com/1420-3049/26/14/4264.

45 A. Jasim, S. Abdelghany and K. Greish, Current Update on the Role of Enhanced Permeability and Retention Effect in Cancer Nanomedicine, in *Nanotechnology-Based Approaches for Targeting and Delivery of Drugs and Genes*, Elsevier, 2017, pp. 62–109, available from: https://linkinghub.elsevier.com/retrieve/pii/B9780128097175000026.

46 Z. Wei, Y. Zhou, R. Wang, J. Wang and Z. Chen, Aptamers as Smart Ligands for Targeted Drug Delivery in Cancer Therapy, *Pharmaceutics*, 2022, **14**(12), 2561. Available from: https://www.mdpi.com/1999-4923/14/12/2561.

47 B. Todaro, E. Ottalagana, S. Luin and M. Santi, Targeting Peptides: The New Generation of Targeted Drug Delivery Systems, *Pharmaceutics*, 2023, **15**(6), 1648.

48 A. A. Attama, P. O. Nnamani, O. B. Onokala, A. A. Ugwu and A. L. Onugwu, Nanogels as target drug delivery systems in cancer therapy: A review of the last decade, *Front. Pharmacol*, 2022, **13**, 874510. Available from: https://www.frontiersin.org/articles/10.3389/fphar.2022.874510/full.

49 T. J. Collins, ImageJ for Microscopy, *BioTechniques*, 2007, **43**(sup1), S25–S30. Available from: https://www.tandfonline.com/doi/full/10.2144/000112517.